Increment of heat transfer by graphene-oxide and molybdenum-disulfide nanoparticles in ethylene glycol solution as working nanofluid in penetrable moveable longitudinal fin

Article *in* Waves in Random and Complex Media · January 2022

CITATIONS
0

READS
326

7 authors, including:

Nabil Talbi
Université 20 août 1955-Skikda
12 PUBLICATIONS **111** CITATIONS
SEE PROFILE

Kezzar Mohamed
60 PUBLICATIONS **518** CITATIONS
SEE PROFILE

Tabet Ismail
Université 20 août 1955-Skikda
67 PUBLICATIONS **504** CITATIONS
SEE PROFILE

Mohamed Rafik Sari
Badji Mokhtar - Annaba University
58 PUBLICATIONS **461** CITATIONS
SEE PROFILE

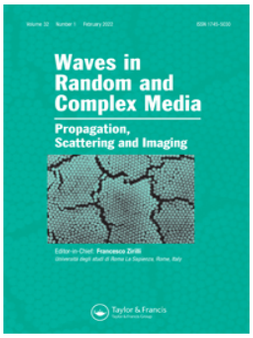

Waves in Random and Complex Media

ISSN: (Print) (Online) Journal homepage: https://www.tandfonline.com/loi/twrm20

Increment of heat transfer by graphene-oxide and molybdenum-disulfide nanoparticles in ethylene glycol solution as working nanofluid in penetrable moveable longitudinal fin

Nabil Talbi, Mohamed Kezzar, Manuel Malaver, Ismail Tabet, Mohamed Rafik Sari, Abderrezak Metatla & Mohamed R. Eid

To cite this article: Nabil Talbi, Mohamed Kezzar, Manuel Malaver, Ismail Tabet, Mohamed Rafik Sari, Abderrezak Metatla & Mohamed R. Eid (2022): Increment of heat transfer by graphene-oxide and molybdenum-disulfide nanoparticles in ethylene glycol solution as working nanofluid in penetrable moveable longitudinal fin, Waves in Random and Complex Media, DOI: 10.1080/17455030.2022.2026527

To link to this article: https://doi.org/10.1080/17455030.2022.2026527

Published online: 31 Jan 2022.

WAVES IN RANDOM AND COMPLEX MEDIA
https://doi.org/10.1080/17455030.2022.2026527

Taylor & Francis
Taylor & Francis Group

Increment of heat transfer by graphene-oxide and molybdenum-disulfide nanoparticles in ethylene glycol solution as working nanofluid in penetrable moveable longitudinal fin

Nabil Talbi[a], Mohamed Kezzar[a], Manuel Malaver[b,c], Ismail Tabet[d], Mohamed Rafik Sari[e], Abderrezak Metatla[a] and Mohamed R. Eid [f,g]

[a]Mechanical Engineering Department, University of 20 aout 1955, Skikda, Algeria; [b]Bijective Physics Institute, Idrija, Slovenia; [c]Department of Basic Sciences, Maritime University of the Caribbean, Catia la Mar, Venezuela; [d]Physical Engineering Department, University of 20 aout 1955, Skikda, Algeria; [e]Laboratory of Industrial Mechanics, Badji Mokhtar University of Annaba, Sidi Amar Annaba, Algeria; [f]Department of Mathematics, Faculty of Science, New Valley University, El-Kharga, Al-Wadi Al-Gadid, Egypt; [g]Department of Mathematics, Faculty of Science, Northern Border University, Arar, Saudi Arabia

ABSTRACT

The main interest of the current research study is, on the one hand, to increase heat transfer of the base and mixture fluids by using hybrid nanoparticles. By considering two types of boundary conditions such as insulated and convective tips, to explore numerically and analytically the simultaneous impacts of the thermal radiative and free convective flow of hybrid nanofluid via a moving porous longitudinal fin. This investigation employs Darcy's model and the mixture base fluid H_2O (50%)–$C_2H_6O_2$ (50%). The governing equations have been solved by utilizing Runge–Kutta–Fehlberg 4th–5th order technique (RKFT45) with shooting-scheme and analytically via Duan–Rach Approach (DRA). It is found that the nondimensional temperature $\theta(\eta)$ is a decreasing function of a wet porous number m_2 and convective parameter *Nc* for both insulated and convective tips, and as an increasing function of ambient temperature θ_a, Peclet number *Pe* and power index *n*. It is also found that the thermal profile $\theta(\eta)$ presents a decrease for all considered shape factors in the cases of insulated and convective tips boundary conditions. Computational results and those obtainable in the previous works have been used to verify and strengthen the results gained by the analytical DRA technique.

ARTICLE HISTORY
Received 7 August 2021
Accepted 4 January 2022

KEYWORDS
Hybrid nanofluid; insulated and convective tips boundary conditions; thermal radiation; natural convection; Duan–Rach approach; Runge–Kutta–Fehlberg method

1. Introduction

Nowadays, it is highly established that the nanofluid term concerns fluid that contains nanometer-sized particles, called nanoparticles. Nanofluids are thus colloids mainly made of the base fluid and very small nanoparticles (< 100 nm) [1,2]. The nanomolecules utilized in nanoliquids are generally obtained from metals, metals-oxides, carbide, or carbon

CONTACT Mohamed R. Eid m_r_eid@yahoo.com

nanotube [3]. Recently, many researchers interested in nanofluids due to their importance for many applications in several engineering and medical processes, like cancer treatment, cooling of electronic devices, domestic refrigerators, and hybrid-powered engines [4,5]. Alizadeh and Dehghan [6] investigated numerically couple free convective of H_2O-based nanoliquids in a quadrangular hollow. In this investigation, two kinds of nanoliquids, specifically $Al_2O_3-H_2O$ and $CuO-H_2O$ are measured. The obtained governing equations resulting from mathematical modeling are resolved to utilize the finite volume technique. The impacts on the cooling efficacy of the hollow were examined by physical factors of interest as Rayleigh number, nanofluid kind, the volumetric concentration of nanoparticle, and the position of the heat generation. Analytically, Kuznetsov and Nield [7] are interested in the free convection boundary layer flowing of a nanoliquid past a vertical wall. The used nanofluid model takes into account the influences of Brownian and thermophoretic diffusions. The obtained similarity calculations are based on Lewis *Le*, buoyancy-ratio *Nr*, Brownian *Nb*, and thermophoretic diffusion *Nt* numbers. Mintsa et al. [8] are interested in the active thermal conductance capacities of Al_2O_3/H_2O and CuO/H_2O nanoliquids. This study explored the influence of nanoparticle size and temperature. Madhesh et al. [9] inspected experimental heat transport and flowing features of $Ag-C_2H_6O_2$ nanofluid flow past a tube-shaped heat exchanger. Results obtained exposed that the convection heat transmission factor and pressure drop of the considered nanofluid significantly upsurge by the rise in nanoparticles fractional size. Shi et al. [10] have prepared magnetite nanofluid to elaborate the quick heat-conducting channel among a heat absorption and generation. This investigation employs a magnetic approachable remoted control heat transmission method by controlling the material property and outside physical domain. The research work done by Katam et al. [11] explores numerically the influence of wall slips with the presence of nanomaterials in a chemically reactive micropolar liquid stream in a convectively heated surface. Results obtained reveal that the temperature of the nanoliquid is enhanced by 18.5%, the activation energy raises concentration, the drag coefficient decreases as thermal and solutal Grashof numbers increase, and Sherwood number is improved for higher values of the temperature difference and chemical reaction parameters. Narayana et al. [12] developed a mathematical model to investigate the effect of heat source on hydromagnetic three-dimensional chemically reacting couple stress nanoliquid flow over a bidirectional stretched sheet. This investigation mainly shows that the rise in thermal radiation and heat generation parameters enhances significantly the thermal and species boundary layer thickness of the liquid. Furthermore, results obtained show that the heat transfer rate and Skin friction coefficient decrease with the augments of couple stress values. Narayana et al. [13] also conducted a numerical simulation of the three-dimensional flow of a couple of stress Casson nanoliquid flows along a horizontal stretching surface. They found that the temperature of the non-Newtonian couple stress fluid is higher than that of Newtonian viscous fluid. Numerically via the implicit Chebyshev pseudo-spectral method, Abd Elazem and Elgazery [14] studied the unsteady nanoliquid flow near a vertical heated wavy surface with temperature-dependent viscosity. They noticed that, with the increase of variable viscosity parameters, the local skin friction coefficient decreases, and the axial nanoliquid velocity near the wavy surface increases. Also, results obtained show that the Nusselt number decreases with the rise in the magnitude of heat radiation; however, a reverse behavior was observed for the nanoparticle Sherwood number. Hussain et al. [15] are interested in the unsteady shear thinning behavior of nanoliquid flow

over exponential stretching/shrinking cylinder. This contribution explores the significance of wall stress and heat transfer rate. The governing ordinary differential equation arising from mathematical modeling is solved via a powerful numerical technique. Naidu et al. [16] were interested in the influence of thermal radiation and partial slip on the hydromagnetic flow of Jeffery nanofluid containing motile gyrotactic microorganisms over a stretching surface. They established that the Nusselt number augments by enhancing thermal radiation parameter; whereas, a reverse trend was observed by increasing the Richardson number.

More recently, the researcher's community has focused on hybrid nanofluids. This novel category is considered as a new generation of working fluids that is mainly composed of two or more nanomaterials suspended in a base liquid. Incorporating multiple nanoparticles to base fluids aim thus to rectify shortcomings of mono nanofluids. Hybrid nanofluids are used in several scientific and technical sectors, such as coolant processing, medications, heat pipe reduction, cooling, boats for improved performance, and aeronautics. According to the literature, several studies were undertaken on hybrid nanofluids. Through the conducted studies, it has been shown that the hybrid nanofluids enhance significantly heat transfer characteristics of standard liquids like H_2O and ethylene glycol. Sarkar et al. [17] provided a thorough overview of current studies on syntheses, thermo-physical features, heat transport, and pressure drop qualities, prospective uses, and obstacles to hybrid nanofluids. The study was done by Jana et al. [18] mainly focused on the enhancement of the base liquid thermal conductance by the adding of mono and mixture nanoparticles. Ghadikolaei et al. [19] executed an examination showing the effect of magnetic field on flowing contain H_2O-based titanium dioxide–copper hybrid nanoliquid. They demonstrated that the platelet-shaped nanoparticles are more effective compared to the other shapes. Iqbal et al. [20] are interested in the flow of H_2O–SiO_2 nanoliquid and H_2O–MoS_2/SiO_2 mixture nanoliquid through a bent extended surface with the effect of several physical parameters of interest like heat source, shaped-factor, magneto-field, slippery influence, and radiative flowing. They displayed that the flowing changes fastly in the case of a mixture nanoliquid than the flow of a single nanofluid. Nawaz and Nazir [21] considered the flows of MoS_2–$C_2H_6O_2$ and MoS_2/SiO_2–$C_2H_6O_2$ nanofluids. Thermal performance of the studied flows is investigated numerically utilizing the finite element technique. Chu et al. [22] deliberated the role of Lorentz force on mixed convection flowing, including H_2O-based Molybdenum disulfide (MoS_2)–Graphene oxide (GO) mixture nanoliquid via a straight tube with thermal radiative flowing and the shaped-factors impacts of considered nanoparticles. They found that the radiative and shaped-factor meaningfully enhance the speed and temperature, along with the frictional force coefficient and Nusselt amount. Hybrid nanofluid flow over a porous stretching sheet taking into account the influences of viscous dissipation and variable viscosity was investigated by Venkateswarlu and Narayana [23]. They demonstrated that the hybrid nanofluid velocity increases with the augment of λ parameter. Also, results gained reveal that the Nusselt number of viscous fluid is lower than those of the nanofluid and the hybrid nanofluid. Wakif et al. [24] give a detailed report on the thermomigration of tiny/nano-sized particles in the motion of various fluids. A meta-analysis on the significance of either nano or tiny particles exposed to thermophoretic force was exposed. An interesting attempt to study the effect of hybrid nanoparticles like diamond and silica dispersed in ethylene glycol considered as a base fluid in a converging/diverging channel was investigated by Basir et al. [25]. They found that the fluid velocity appears as a

decreasing function of Reynolds number and nanoparticle volume fraction in a diverging channel. They also found that the Skin friction coefficient raises with the augment of diamond nanoparticle fraction for a divergent channel. Ramzan et al. [26] conducted a comparative analysis of the heat transfer performance of hybrid nanofluid and simple nanofluid flows amidst two rotating disks in porous media by considering Darcy–Forchheimer effect. The comparison was done between the numerical 'bvp4c' approach and the statistical response surface method. The influences of various hybrid nanofluids on the unsteady hydromagnetic flow and heat transfer features with the presence of thermal radiation and a temperature-dependent heat source were explored by Rajesh et al. [27]. They demonstrated that the rise in the magnitude of the average Nusselt number mainly occurs with the augment of nanoparticle volume fraction.

The main aim of this investigation work is to scrutinize the simultaneous impacts of thermal radiative and natural convection on the flowing of a hybrid nanofluid (H_2O–$C_2H_6O_2$/GO–MoS_2) over a moving porous longitudinal fin by considering two types of boundary conditions such as insulated and convective tips. Darcy's model is used and the nonlinear governing equation of the studied problem was resolved numerically through RKFT45 featuring shooting method and analytically with the aid of a robust modified method of decomposition namely the Duan–Rach approach. The effect of several physical parameters such as Peclet number, convection, radiation parameters, power index number, wet penetrable factor, dimensionless surrounding temperature, and Biot number was explored. The present investigation is thus systematized as next: in Section 2 are presented the governing equations of the considered hybrid nanofluid flow; in Section 3 we used the modified Duan–Rach–Adomian decomposition method to solve analytically the nonlinear differential equation arising from mathematical modeling; in Section 4 we are interested in the main results with detailed discussions. Finally, Section 5 is dedicated to the main conclusions.

2. Governing equations

We consider the flowing of mixture nanoliquid over longitudinal rectangular movable fin with constant area A and length L. The fin was primarily at rest with T_a and T_b are respectively the ambient and base temperatures. The geometrical configuration of the considered problem is represented in Figure 1. It is supposed that the fin is penetrable and consequently Darcy model is adopted. Furthermore, the longitudinal fin is surrounded by a mixture of base fluid H_2O (50%)–$C_2H_6O_2$ (50%) and hybrid nanoparticles (GO–MoS_2).

The following assumptions were considered in the system strategy:

(1) With time and the fin's temperature, the heat flux leftovers are fixed (i.e. invariable with time).
(2) The average temperature is unified around the fin.
(3) There is nothing that resists touching when the base of the fin reaches the main surface.
(4) The temperature of the base fin is consolidated (i.e. uniform).
(5) Compared to its breadth and length, the thickness of the fin is small so that temperature variations by the thickness of the fine edges and thermal transfer are small than with heat that exits the lateral surface.

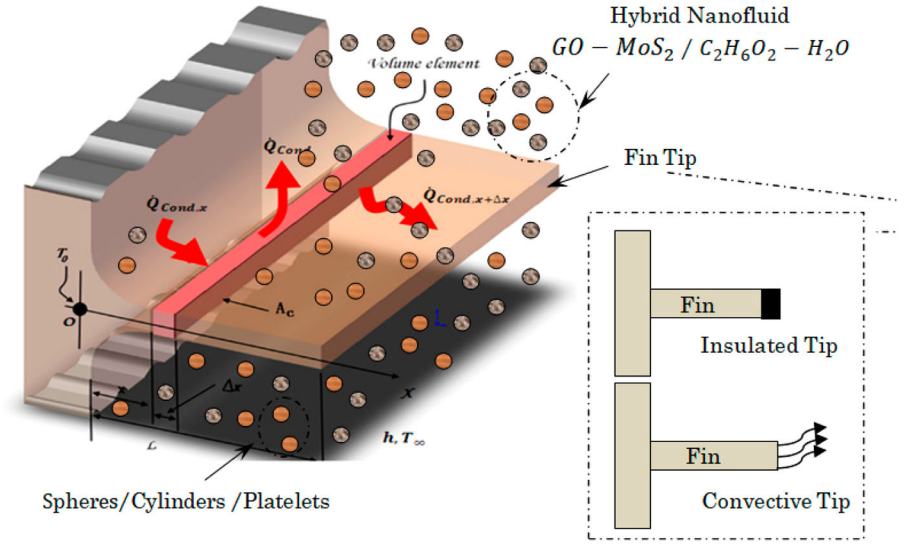

Figure 1. Physical model.

(6) The mixture nanoparticles and the continuity fluid phase are thermally balanced (i.e. in a state of thermal equilibrium).
(7) Two kinds of border constraints were taken into accounts, such as the insulated and convective tips.

The energy balance formula of the longitudinal fin with mixture nanofluid (H_2O–$C_2H_6O_2$ /GO–MoS_2) flowing at a small cross-section is as follows:

$$\frac{d^2T}{dx^2} - \frac{(\rho Cp)_{hnf}U}{k_{hnf}}\frac{dT}{dx} - \frac{2h_D i_{fg}(1-\bar{\varphi})(\omega-\omega_a)}{k_{hnf}t} - \frac{2h(1-\bar{\varphi})(T-T_a)}{k_{hnf}t} - \frac{2gK(\rho Cp)_{hnf}(\rho\beta)_{hnf}}{\mu_{hnf}k_{hnf}t}(T-T_a)^2 - \frac{2\varepsilon\sigma F_{f-a}}{k_{hnf}t}(T^4 - T_a{}^4) = 0. \tag{1}$$

Subject to the following boundary conditions:

- For insulated-tip constraint:

$$\text{at } x = 0 \rightarrow T(0) = T_b,$$
$$\text{at } x = L \rightarrow \frac{dT(L)}{dx} = 0. \tag{2}$$

- For convective-tip constraint:

$$\text{at } x = 0 \rightarrow T(0) = T_b,$$
$$\text{at } x = L \rightarrow k_{hnf}\frac{dT(L)}{dx} + h_a T(L) = 0. \tag{3}$$

The quantities $\rho_{hnf}, \mu_{hnf}, C_{p_{hnf}}, k_{hnf}$ and β_{hnf} are the density, dynamical viscidness, specifical heat at a fixed pressure, thermal conductivity, and volumetric coefficient of thermal expansion of the hybrid nanofluid respectively.

The above mentioned properties of the hybrid nanofluid are expressed as follows

$$
\begin{aligned}
\nu_{hnf} &= \frac{\mu_{hnf}}{\rho_{hnf}},\\
\mu_{hnf} &= \frac{\mu_f}{(1-\varphi_1)^{2.5}(1-\varphi_2)^{2.5}},\\
\rho_{hnf} &= \rho_f\left((1-\varphi_2)\left((1-\varphi_1)+\varphi_1\frac{\rho_{p1}}{\rho_f}\right)+\varphi_2.\frac{\rho_{p2}}{\rho_f}\right),\\
(\rho\beta)_{hnf} &= (\rho\beta)_f(1-\varphi_2)\left((1-\varphi_1)+\varphi_1\frac{(\rho\beta)_{p1}}{(\rho\beta)_f}\right)+\varphi_2(\rho\beta)_{p2},\\
(\rho Cp)_{hnf} &= (\rho Cp)_f(1-\varphi_2)\left((1-\varphi_1)+\varphi_1\frac{(\rho Cp)_{p1}}{(\rho Cp)_f}\right)+\varphi_2(\rho Cp)_{p2},\\
k_{hnf} &= \left(\frac{k_{p2}+(m-1)k_{bf}-(m-1)\varphi_2(k_{bf}-k_{p2})}{k_{p2}+(m-1)k_{bf}+\varphi_2(k_{bf}-k_{p2})}\right)k_{bf},\\
k_{bf} &= \left(\frac{k_{p1}+(m-1)k_f-(m-1)\varphi_1(k_f-k_{p1})}{k_{p1}+(m-1)k_f+\varphi_1(k_f-k_{p1})}\right)k_f,
\end{aligned}
\tag{4}
$$

where m is the shaped-factor of the considered solid nanoparticles. In this investigation, several shapes like sphere, cylinder, and platelet of nanoparticles were considered. Table 1 depicts different particles shapes.

Table 2 displays thermo-physical attributes of the pure ($C_2H_6O_2$–H_2O) standard liquid and solid nanomolecules (GO and MoS_2).

The heat transmission factor h is presumed as a temperature function and specified as

$$
h = h_a\left(\frac{T-T_a}{T_b-T_a}\right)^n. \tag{5}
$$

Table 1. Shape factor of solid nanoparticles.

Nanoparticles type	Shape	Shape factor
Sphere		$m = 3$
Cylinder		$m = 4.9$
Platelet	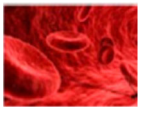	$m = 5.7$

Table 2. Thermo-physical attributes of mixture standard liquid and nanomolecules [28–30].

Physical properties	ρ(kg/m^3)	C_p(J/kg $\cdot^\circ$ K)	k(W/m $\cdot^\circ$ K)	β(1/$^\circ$K)
$C_2H_6O_2$–H_2O	1063.8	3630	0.387	5.8×10^{-4}
GO	1800	717	5000	2.84×10^{-4}
MoS_2	5060	397.21	904.4	2.8424×10^{-5}

By using the following similarity transformation:

$$\begin{aligned} \eta &= x/L, \\ \theta &= T/T_a, \\ \theta_a &= T_a/T_b, \\ (\omega - \omega_a) &= b_2(T - T_a), \end{aligned} \tag{6}$$

and after some simplifications, we obtain the following dimensionless form:

$$\frac{d^2\theta}{d\eta^2} - Pe\left(\frac{(\rho Cp)_{hnf}}{(\rho Cp)_f}\right)\left(\frac{k_f}{k_{hnf}}\right)\frac{d\theta}{d\eta} - Nc\left(\frac{(\rho Cp)_{hnf}}{(\rho Cp)_f}\right)\left(\frac{(\rho\beta)_{hnf}}{(\rho\beta)_f}\right)\left(\frac{k_f}{k_{hnf}}\right)(1-\varphi_1)^{2.5}$$
$$(1-\varphi_2)^{2.5}(\theta-\theta_a)^2 - m_2\left(\frac{k_f}{k_{hnf}}\right)\frac{(\theta-\theta_a)^{1+n}}{(1-\theta_a)^n} - Nr\left(\frac{k_f}{k_{hnf}}\right)(\theta^4 - {\theta_a}^4) = 0. \tag{7}$$

Accordingly, in terms of $\theta(\eta)$, the appropriate bounder constraints for the considered system are specified as:

- For insulated-tip constraint:

$$\begin{aligned} &\text{at } \eta = 0 \rightarrow \theta(0) = 1, \\ &\text{at } \eta = 1 \rightarrow \theta'(1) = 0. \end{aligned} \tag{8}$$

- For convective-tip constraints:

$$\begin{aligned} &\text{at } \eta = 0 \rightarrow \theta(0) = 1, \\ &\text{at } \eta = 1 \rightarrow \theta'(1) = -\frac{k_f}{k_{hnf}}B_i\theta(1), \end{aligned} \tag{9}$$

where η is the dimensionless axial distance, $B_i = Lh_a/k_f$ is the Biot number, $Pe = (\rho Cp)_f UL/k_f$ is the Peclet number, $m_2 = \underbrace{2h_aL^2(1-\bar{\varphi})/k_ft}_{m_0} + \underbrace{2h_aL^2i_{fg}(1-\bar{\varphi})b_2/k_ftCp_fLe^{2/3}}_{m_1}$ is the wet porous number, $Nc = 2(\rho\beta)_f gK(\rho Cp)_f T_b L^2/\mu_f k_f t$ is the convective number, $Nr = 2\varepsilon\sigma L^2{T_b}^3/k_f t$ is the radiation parameter, n is the power index, θ_a is the nondimensional surrounding temperature and θ is the nondimensional temperature.

3. Employment of DRA method

The nonlinear differential equation (Equation (7)) governing the studied problem with the boundary conditions (8) and (9) has been treated analytically using the modified Duan–Rach–Adomian decomposition method [31]. Recently, this robust modified technique of computation was successfully employed for solving many physical problems [32–35].

According to the DRA algorithm [31], Equation (7) can be written as:

$$\mathcal{L}\theta'' = -\left\langle -Pe\cdot A_1\cdot A_2\theta' - Nc\cdot A_1\cdot A_2\cdot A_3(1-\varphi_1)^{2.5}(1-\varphi_2)^{2.5}(\theta-\theta_a)^2 - m_2\cdot A_2\frac{(\theta-\theta_a)^{1+n}}{(1-\theta_a)^n} - Nr\cdot A_2(\theta^4-{\theta_a}^4)\right\rangle, \tag{10}$$

here the differential-operator $\mathcal{L}$ and the inverse operator $\mathcal{L}^{-1}$ are specified respectively by

$$\mathcal{L}_\theta = \frac{\mathrm{d}^2}{\mathrm{d}\eta^2},$$
$$\mathcal{L}_\theta{}^{-1}(\blacksquare) = \int_0^\eta\int_0^\eta(\blacksquare)d\eta d\eta. \tag{11}$$

With:

$$A_1 = \left(\frac{(\rho Cp)_{hnf}}{(\rho Cp)_f}\right),$$
$$A_2 = \left(\frac{k_f}{k_{hnf}}\right),$$
$$A_3 = \left(\frac{(\rho\beta)_{hnf}}{(\rho\beta)_f}\right). \tag{12}$$

Effective with $\mathcal{L}^{-1}$ on Equation (10) and after applying bounder constraints on it, we get

$$\theta(\eta)-\theta(0)-\eta\theta'(0) = -\mathcal{L}^{-1}\left\langle -Pe\cdot A_1\cdot A_2\theta' - Nc\cdot A_1\cdot A_2\cdot A_3(1-\varphi_1)^{2.5}(1-\varphi_2)^{2.5}(\theta-\theta_a)^2\cdot m_2\cdot A_2\frac{(\theta-\theta_a)^{1+n}}{(1-\theta_a)^n} - Nr\cdot A_2(\theta^4-{\theta_a}^4)\right\rangle. \tag{13}$$

By putting $\eta = 1$ in Equation (11), we obtain:

$$\theta'(0) = a - 1 + \int_0^1\int_0^\eta\left\langle -Pe\cdot A_1\cdot A_2\theta' - Nc\cdot A_1\cdot A_2\cdot A_3(1-\varphi_1)^{2.5}(1-\varphi_2)^{2.5}(\theta-\theta_a)^2\right.$$

$$+ m_2 \cdot A_2 \frac{(\theta-\theta_a)^{1+n}}{(1-\theta_a)^n} - Nr \cdot A_2(\theta^4 - {\theta_a}^4)\Bigg\rangle. \tag{14}$$

Substituting Equation (14) into Equation (13) yields

$$\begin{aligned}\theta(\eta) = 1 - \eta + a\eta + \eta \int_0^1 \int_0^\eta \Bigg\langle & - Pe \cdot A_1 \cdot A_2 \theta' - Nc \cdot A_1 \cdot A_2 \\ & \cdot A_3 (1-\varphi_1)^{2.5}(1-\varphi_2)^{2.5}(\theta-\theta_a)^2 \\ & - m_2 \cdot A_2 \frac{(\theta-\theta_a)^{1+n}}{(1-\theta_a)^n} - Nr \cdot A_2(\theta^4 - {\theta_a}^4)\Bigg\rangle d\eta d\eta \\ & - \int_0^\eta \int_0^\eta \Bigg\langle - Pe \cdot A_1 \cdot A_2 \theta' - Nc \cdot A_1 \cdot A_2 \cdot A_3 (1-\varphi_1)^{2.5}(1-\varphi_2)^{2.5}(\theta-\theta_a)^2 \\ & - m_2 \cdot A_2 \frac{(\theta-\theta_a)^{1+n}}{(1-\theta_a)^n} - Nr \cdot A_2(\theta^4 - {\theta_a}^4)\Bigg\rangle d\eta d\eta,\end{aligned}$$

where $\theta_0(\eta)$ is given by:

$$\theta_0(\eta) = 1 - \eta + a\eta \tag{15}$$

After performing the above iterative method, the first component areas are obtained as follows (for $n = 1$):

$$\begin{aligned}\theta_1(\eta) = & -\frac{1}{-1+\theta_a} A_2 \Big(-\frac{1}{5}(-1+a)^3 Nr\eta^5(-1+\theta_a) - \frac{1}{30}(-1+a)^4 Nr\eta^6(-1+\theta_a) \\ & - \frac{1}{12}(-1+a)^2 Nc\eta^4 A_1 A_3 A_4(-1+\theta_a) - \frac{1}{3}(-1+a)\eta^3(2Nr+m_2)(-1+\theta_a) \\ & + \frac{1}{3}(-1++a)Nc\eta^3 A_1 A_3 A_4(-1+\theta_a)^2 + \frac{1}{12}(-1+a)^2\eta^4(6Nr+m_2-6Nr\theta_a) \\ & - \frac{1}{2}\eta^2 A_1(-1+\theta_a)(-Pe+aPe+NcA_3A_4 - 2NcA_3A_4\theta_a + NcA_3A_4\theta_a^2) \\ & + \frac{1}{2}\eta^2(-1+\theta_a)^2(Nr+m_2+Nr\theta_a+Nr\theta_a^2+Nr\theta_a^3)) \\ & + \frac{1}{60(-1+\theta_a)}\eta A_2(5m_2(3+a(2+a)-4(2+a)\theta_a+6\theta_a^2) \\ & - 2Nr(-1+\theta_a)(5+a(4+a(3+a(2+a)))) - 15\theta_a^4) \\ & - 5A_1(-1+\theta_a)(6(-1+a)Pe \\ & + NcA_3A_4(3+a(2+a)-4(2+a)\theta_a+6\theta_a^2))).\end{aligned} \tag{16}$$

By using the boundary conditions (8) and (9), the constant a could be determined as follows:

- For insulated-tip condition:

$$\theta'(1) = 0 \tag{17}$$

- For convective coefficient at the tip:

$$\theta'(1) = -\frac{k_f}{k_{hnf}} B_i \theta(1). \tag{18}$$

Lastly, the approximate solution to the problem examined may be expressed as:

$$\theta_n(\eta) = \theta_1(\eta) + \theta_2(\eta) + \theta_3(\eta) + \theta_4(\eta) + \ldots + \theta_m(\eta). \tag{19}$$

4. Results and discussions

This investigation is interested in the thermal performance of moving longitudinal porous fin under-insulated and convective tips boundary conditions in the existence of free convective and radiative flowing. The resultant ODEs sideways with the adopted bounder constraints were resolved numerical and analytical with the help of the RKFT45 and Duan–Rach Approach respectively. It is worth noting that, in the parametric study showing the evolution of thermal distribution, we have varied each influencing parameter separately by keeping all other physical parameters fixed. In fact, for the studied cases displayed in Figures 2–6, the following fixed parameters are considered $n = 1, m = 3, \varphi_{GO} = \varphi_{MoS_2} = 2\%, m_2 = 1, Pe = 0.5$ and $Bi = 1$.

The evolution of dimensionless temperature $\theta(\eta)$ for different values of radiation parameter Nr for together convective and insulated tips bounder constraints when $Nc = 0.5$ and $Pe = 0.5$ are displayed in Figure 2. It is highly remarked that the dimensionless temperature $\theta(\eta)$ decreases with the rise in the magnitude of the radiative parameter Nr for both considered boundary conditions. It is worth noting that a small decrease in the temperature magnitude is noticed with the rise of Nr parameter in the case of a convective tip.

Figure 3 displays the temperature evolution under the effect of varying the convective parameter Nc when $Nr = 2$ and $Pe = 1$. In fact, for the same two boundary conditions, convective and insulated tip, the dimensionless temperature $\theta(\eta)$ appears as a decreasing function versus the Nc parameter. For these cases, it is highly observed that the rise of Nc parameter exhibits little effect on the behavior of thermal distribution. It is noteworthy that the upsurge in convection parameter Nc makes low the temperature of the fin surface due to the natural convection phenomenon.

The behavior of dimensionless temperature $\theta(\eta)$ versus wet porous number m_2 for both convective tip and insulated tip conditions was studied and visualized by Figure 4 when the radiation parameter and convective parameter are kept fixed at $Nr = 0.2$ and $Nc = 2$. For the insulated tip, results obtained reveal that $\theta(\eta)$ diminishes significantly with increasing wet porous parameter m_2; however, for a convective tip, a gradual decrease in the magnitude of $\theta(\eta)$ was observed with the increase of wet porous number. In fact, due to the decrease in fin temperature, the wet penetrable surface of the fin mainly improves the heat transmission from the fin surface.

As drawn in Figure 5, the behavior of thermal distribution under the influence of Peclet number Pe when $Nr = 1$ and $Nc = 1$ were investigated for both insulated and convective tips. Results obtained show a significant increase in the magnitude of dimensionless temperature $\theta(\eta)$ with the augment of Peclet number Pe. The increase in the magnitude of Peclet number is caused by the increase in the moving fin velocity. This increase in velocity

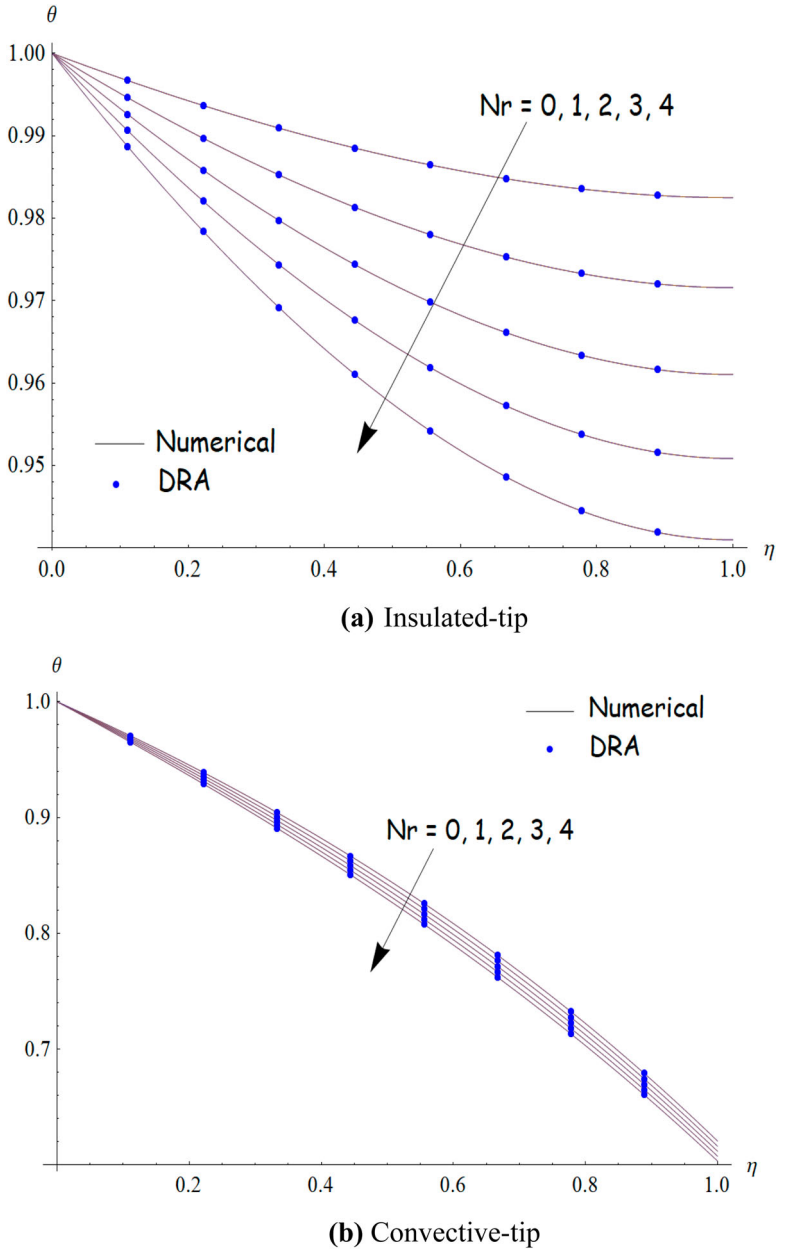

Figure 2. Dimensionless temperature $\theta(\eta)$ for diverse amounts of radiation parameter *Nr* for (a) insulated-tip boundary constraint, (b) convective-tip boundary constraint when $n = 1, m = 3, \varphi_{GO} = \varphi_{MoS_2} = 2\%, m_2 = 1, Nc = 0.5, \theta_a = 0.2, Pe = 0.5$, and $Bi = 1$.

reduces considerably the interacting time among the fin and nearby. In this situation, heat transmission diminishes with the augment of *Pe*. Consequently, the fin temperature augments.

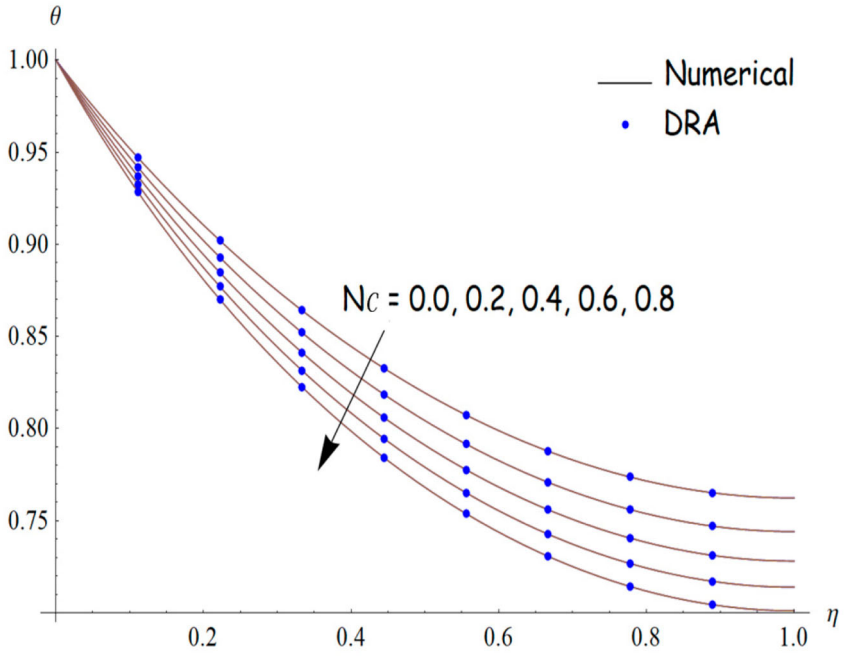

(a) Insulated-tip

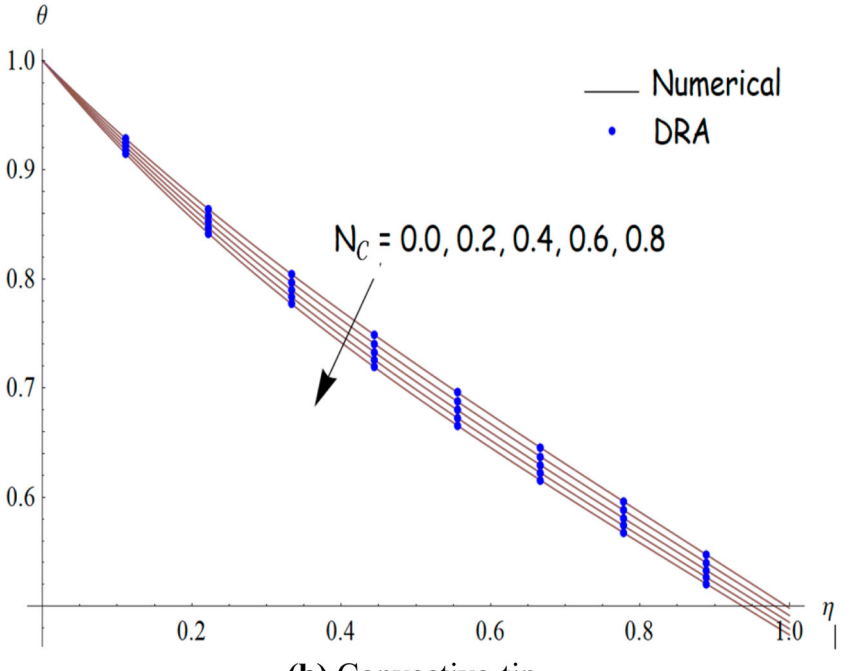

(b) Convective-tip

Figure 3. Dimensionless temperature $\theta(\eta)$ for diverse amounts of the convective parameter *Nc* for (a) insulated-tip boundary constraint, (b) convective-tip boundary constraint when:$n = 1, m = 3, \varphi_{GO} = \varphi_{MoS_2} = 2\%, m_2 = 1, Nr = 2, \theta_a = 0.2, Pe = 1$, and $Bi = 1$.

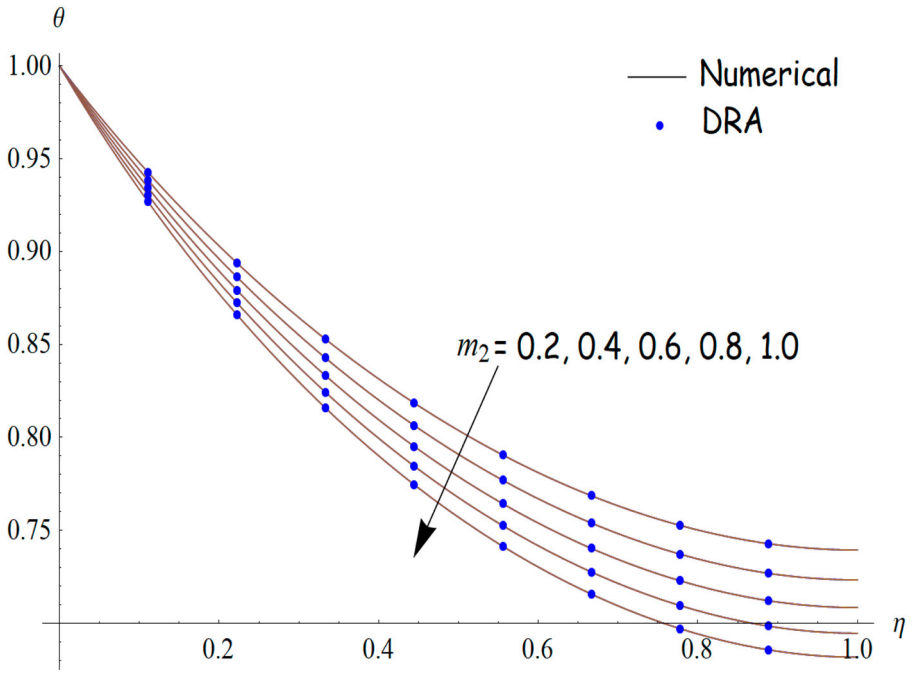

(a) Insulatedtip

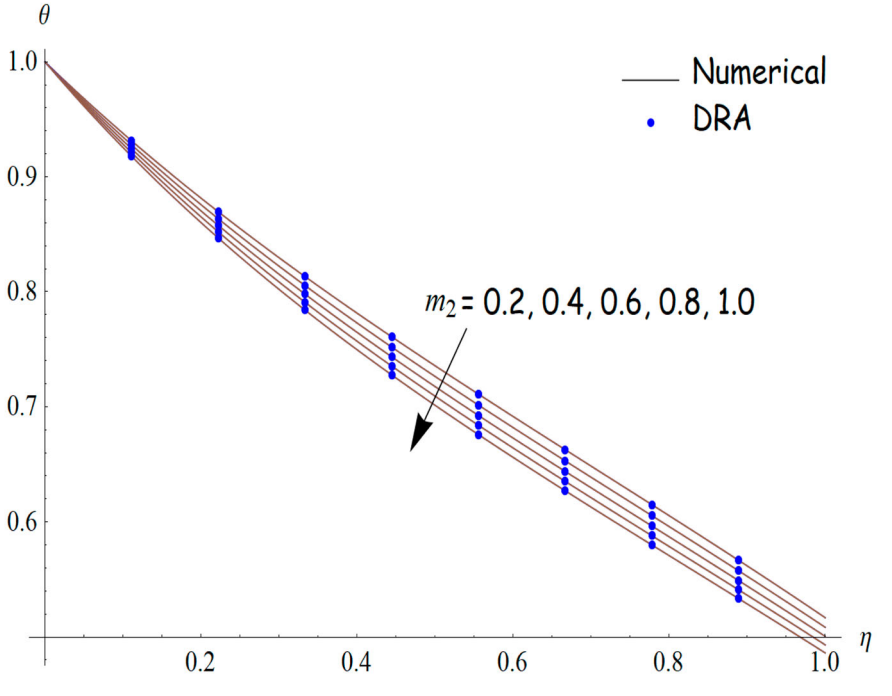

(b) Convective tip

Figure 4. Dimensionless temperature $\theta(\eta)$ for diverse amounts of wet porous parameter m_2 for (a) insulated-tip boundary constraint, (b) convective-tip boundary constraint when $n = 1, m = 3, \varphi_{GO} = \varphi_{MoS_2} = 2\%, Nc = 2, Nr = 0.2, \theta_a = 0.2, Pe = 1$, and $Bi = 1$.

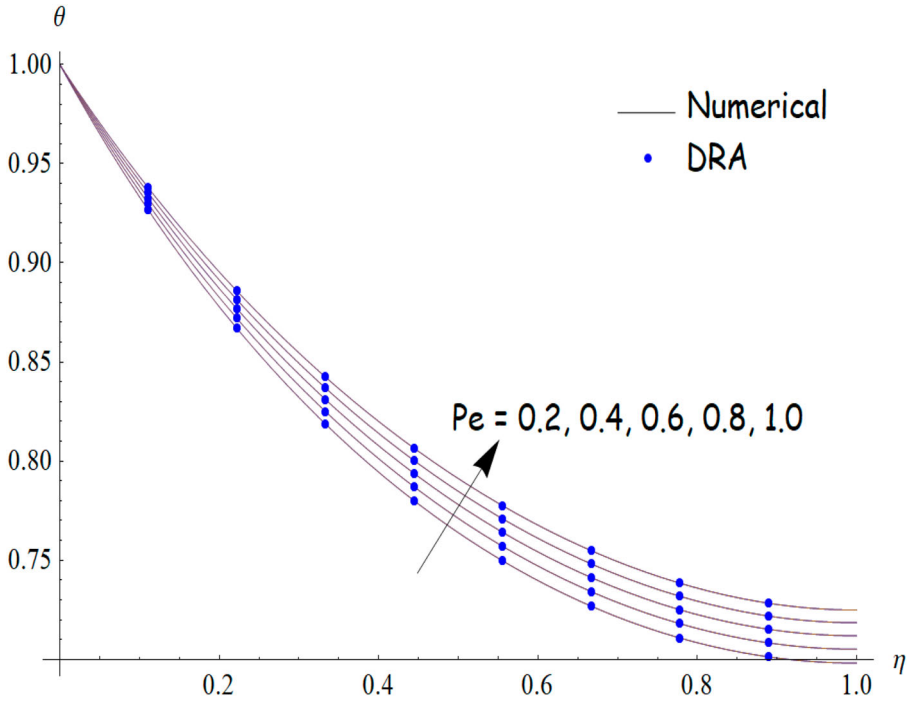

(a) Insulated-tip

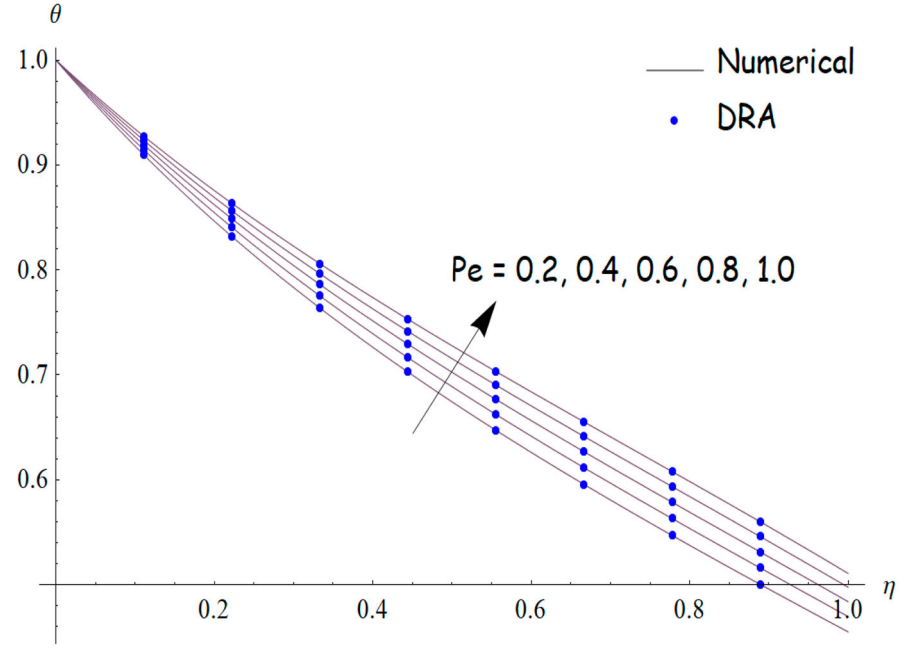

(b) Convective-tip

Figure 5. Dimensionless temperature $\theta(\eta)$ for different values of the Peclet number *Pe* for (a) insulated-tip boundary constraint, (b) convective-tip boundary constraint when: $n = 1, m = 3, \varphi_{GO} = \varphi_{MoS_2} = 2\%, Nc = 1, Nr = 1, \theta_a = 0.2, m_2 = 1$, and $Bi = 1$.

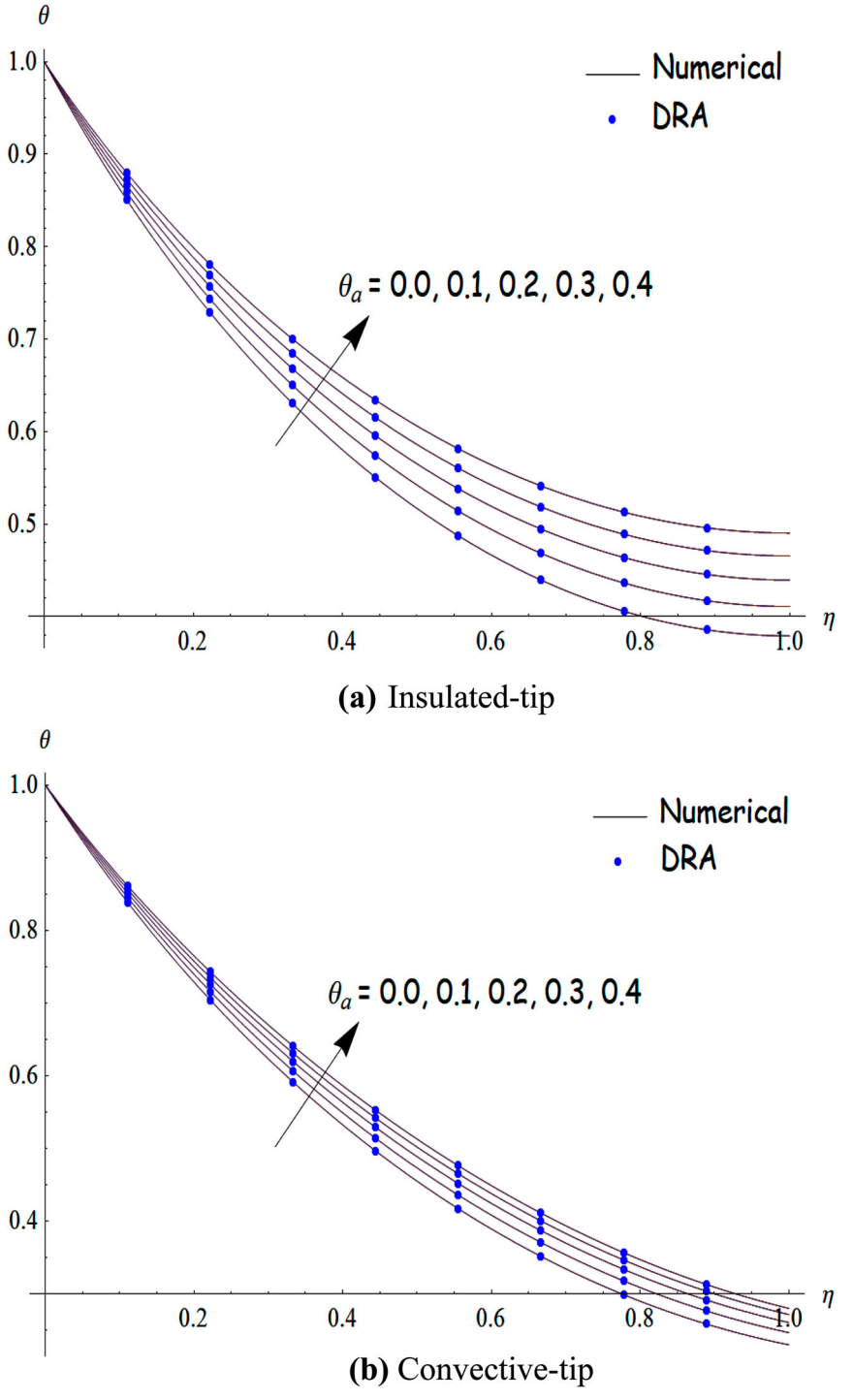

Figure 6. Dimensionless temperature profile $\theta(\eta)$ for diverse amounts of the ambient temperature θ_a for (a) insulated-tip boundary constraint, (b) convective-tip boundary constraint when $n = 1$, $m = 3, \varphi_{GO} = \varphi_{MoS_2} = 2\%, Nc = 1, Nr = 1, \theta_a = 0.2, m_2 = 1$, and $Bi = 1$.

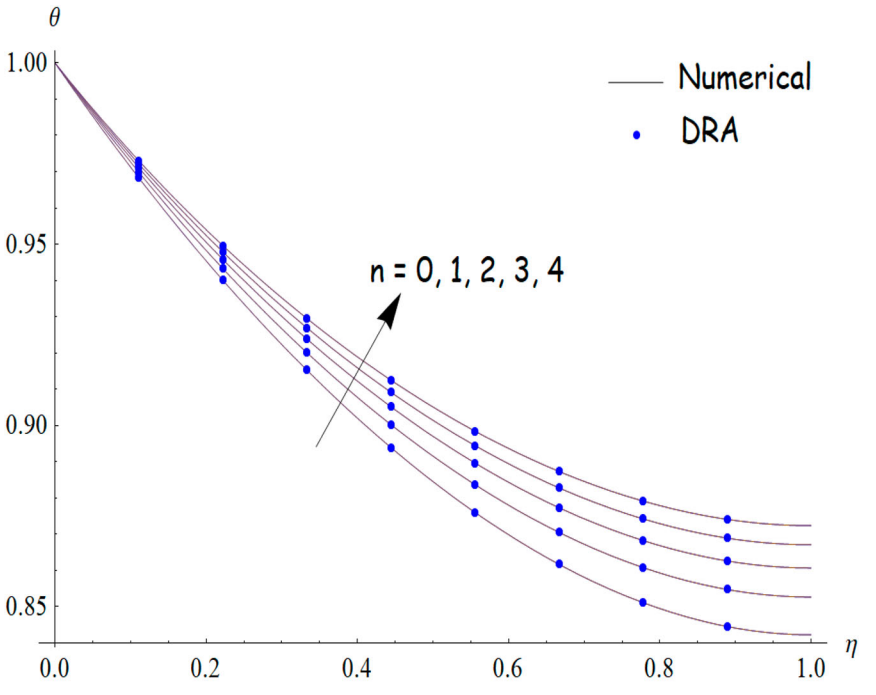

(a) Insulated-tip

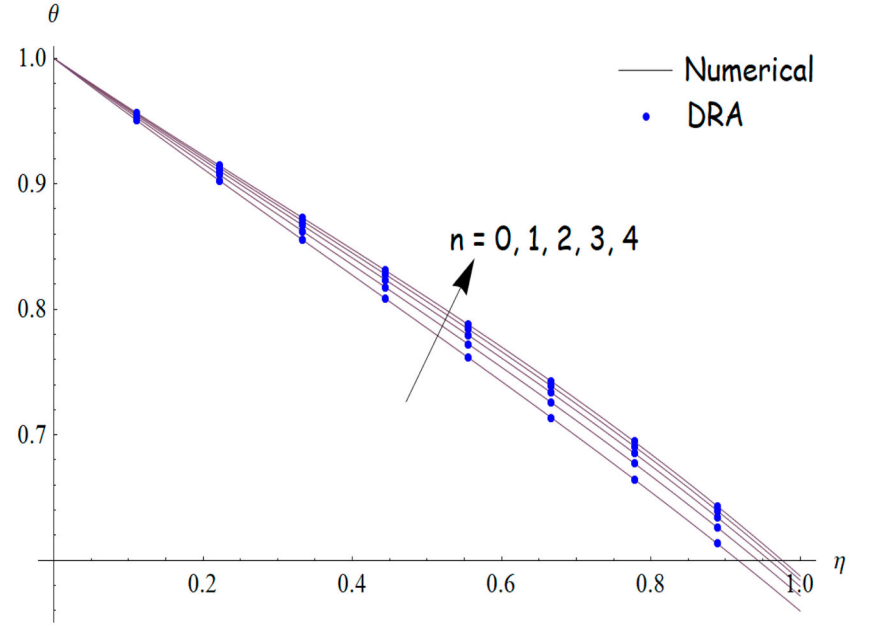

(b) Convective-tip

Figure 7. Dimensionless temperature $\theta(\eta)$ for diverse amounts of power index parameter n for (a) insulated-tip boundary constraint, (b) convective-tip boundary constraint when $m = 3, \varphi_{GO} = \varphi_{MoS_2} = 2\%, Nc = Nr = \theta_a = 0.2, m_2 = 0.4, Pe = 1$, and $Bi = 1$.

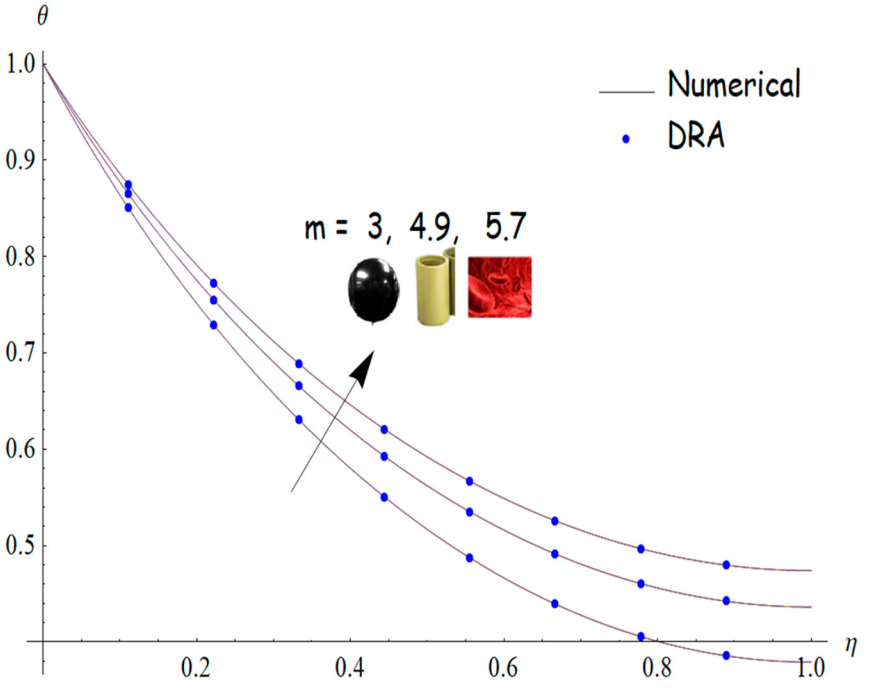

(a) Insulated-tip

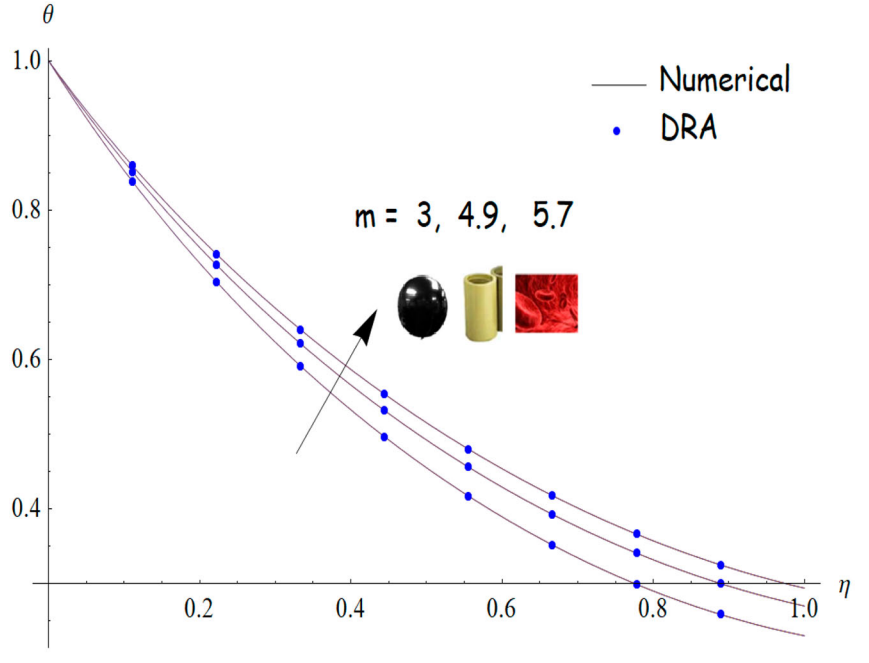

(b) Convective-tip

Figure 8. Dimensionless temperature $\theta(\eta)$ for diverse amounts of shape factor m for (a) insulated-tip boundary constraint, (b) convective-tip boundary constraint when $n = 1, \varphi_{GO} = \varphi_{MoS_2} = 2\%, Nc = 1, Nr = 1, \theta_a = 0.2, m_2 = 0.6, Pe = 1$, and $Bi = 1$.

The dependence of dimensionless temperature $\theta(\eta)$ on the ambient temperature θ_a is drawn in Figure 6. In this case, the temperature profile $\theta(\eta)$ appears as an increasing function with the increase of the ambient temperature θ_a for both convective and insulated tips conditions. This means that the heat transit from the fin flatness to the environment decreases as the ambient temperature augments.

Figure 7 shows the effect of power index factor *n* on the behavior of thermal distribution when $m = 3, \varphi_{GO} = \varphi_{MoS_2} = 2\%, m_2 = 0.4, N_c = 0.2, N_r = 0.2, \theta_a = 0.2, Pe = 1,$ and $Bi = 1$. Results obtained reveal an increase of dimensionless temperature $\theta(\eta)$ with the rise in the magnitude of power index *n* for the status of convective-tip bounder constraints; whereas, for the insulated-tip boundary condition, results reveal that the temperature magnitude increases considerably as the power index *n* augment. The less value of the power index means that the fin temperature is low. Also, from Figure 8, the dimensionless temperature $\theta(\eta)$ exhibits a significant increase with the rise in shape factor of the considered solid nanoparticles in both cases of insulated and convective tips boundary conditions. Here, we notice that the fin temperature is a smaller amount for spheric-shape nanoparticles kept track of cylinder and platelet shape.

The Biot number *Bi* influence on the evolution of thermal distribution in the case of convective-tip boundary condition was depicted by Figure 9. Results obtained reveal that the dimensionless temperature $\theta(\eta)$ considerably declines with the rise of Biot number.

Effect of Peclet number *Pe*, on the heat transit rate $-\theta'(0)$ for some amounts of wet penetrable parameter m_2 in the case of insulated and convective tips of boundary conditions is depicted in Figure 10. Results obtained display that the heat transit rate $-\theta'(0)$

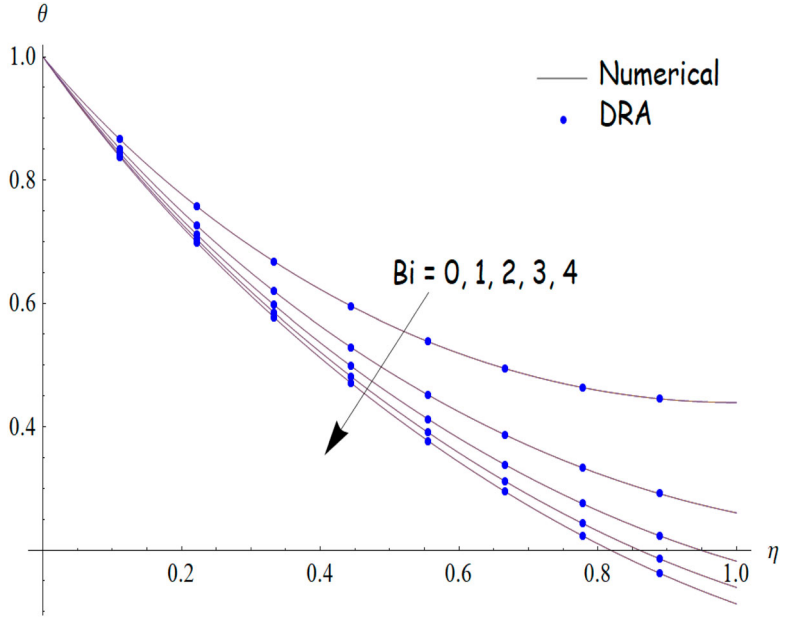

Figure 9. Dimensionless temperature $\theta(\eta)$ for different values of the Biot number *Bi* in the case of convective-tip boundary condition when $n = 1, \varphi_{GO} = \varphi_{MoS_2} = 2\%, Nc = 1, Nr = 1, \theta_a = 0.2, m_2 = 0.6, Pe = 1,$ and $m = 3$.

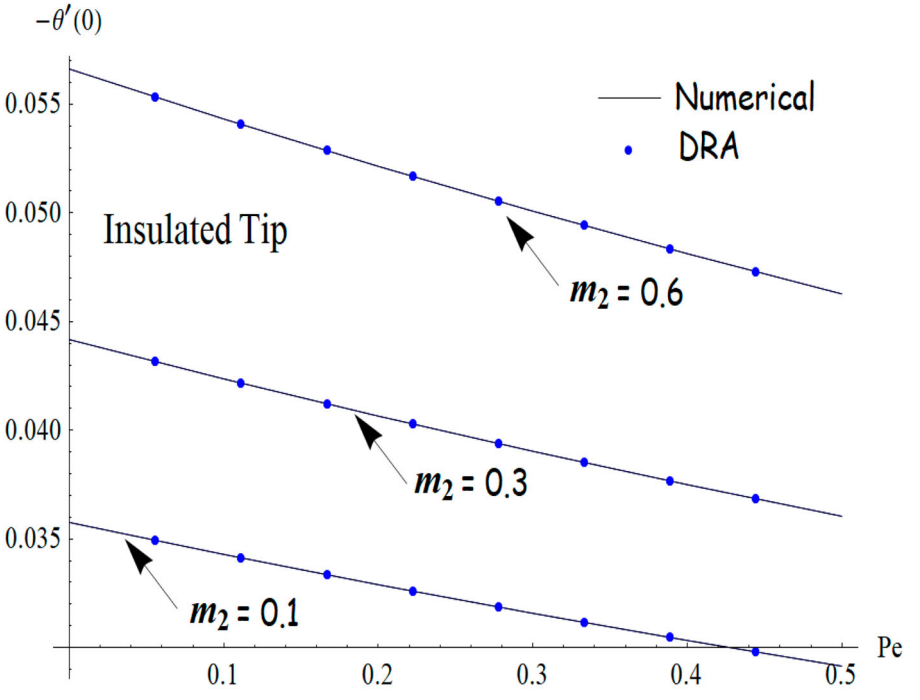

(a) Insulated-tip

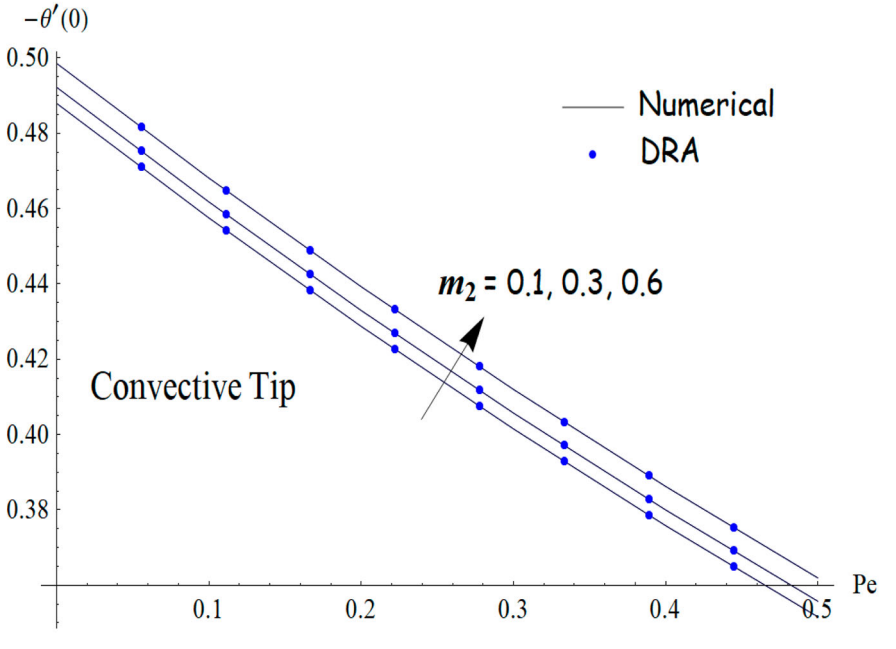

(b) Convective-tip

Figure 10. Heat transmission rate $-\theta'(0)$ for diverse amounts of Peclet number *Pe* and wet porous parameter m_2 for (a) insulated-tip boundary constraint, (b) convective-tip boundary constraint when $n = 1, m = 3, \varphi_{GO} = \varphi_{MoS_2} = 2\%, Nc = 1, Nr = 1, \theta_a = 0.2$, and $Bi = 1$.

diminishes with the augment of Peclet number *Pe*. In the situation of convective-tip boundary condition, this decline is sharpest compared to the situation of insulated-tip bounder constraints.

A comparison between analytical Duan–Rach–Adomian solution, numerical RKFT45 solution, and those obtained by Gireesha et al. [36] was made for dimensionless temperature $\theta(\eta)$ under the effect of Peclet *Pe* number in the case of insulated-tip boundary conditions. The comparison is drawn in Figure 11 and the results obtained are very closer, thus showing the higher accuracy of the adopted DRA technique. On the other hand, Tables 3

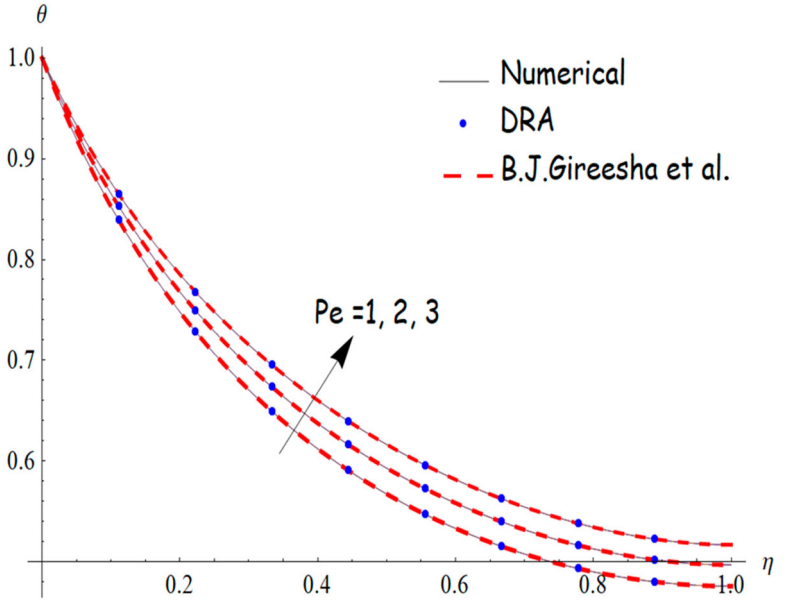

Figure 11. Comparing between DRA solution of $\theta(\eta)$ with numerical results and those available in Ref. [36] for different values of Peclet number *Pe* in the case of insulated-tip boundary constraint when $n = 1, m = 3, \varphi_{GO} = \varphi_{MoS_2} = 4\%, Nc = 10, Nr = 5, \theta_a = 0.2, m_2 = 1$, and $Bi = 1$.

Table 3. Numerical values of $\theta(\eta)$ in the case of insulated-tip boundary conditions when $n = 1, m = 3, \varphi_{GO} = \varphi_{MoS_2} = 2\%, Nc = 1, Nr = 1, \theta_a = 0.2, m_2 = 1$ and $Bi = 1$.

	Insulated tip		
η	$\theta^{\text{RKFT45}}_{\text{Insulated tip}}$	$\theta^{\text{Rach approach}}_{\text{Insulated tip}}$	Error
0.00	1.000000	1.000000	0.0000000
0.10	0.9320313875747194	0.932031376598300	1.09×10^{-8}
0.20	0.8755359984253771	0.875535987654300	1.07×10^{-8}
0.30	0.8284040619506899	0.828404076553200	1.46×10^{-8}
0.40	0.7891703772709692	0.789170359087540	1.81×10^{-8}
0.50	0.7568259137198492	0.756825909854325	3.86×10^{-9}
0.60	0.7307017495950704	0.730701756789000	7.19×10^{-9}
0.70	0.7103974094873465	0.710397412657900	3.17×10^{-9}
0.80	0.6957383564598423	0.695738367548900	1.10×10^{-8}
0.90	0.6867543300411999	0.686754312657090	1.73×10^{-8}
1.00	0.6836744399909099	0.683674443287950	3.29×10^{-9}

Table 4. Numerical values of $\theta(\eta)$ in the case of convective-tip boundary condition when $n = 1, m = 3, \varphi_{GO} = \varphi_{MoS_2} = 2\%, Nc = 1, Nr = 1, \theta_a = 0.2, m_2 = 1$ and $Bi = 1$.

	Convective Tip		
η	$\theta^{\text{RKFT45}}_{\text{Convective tip}}$	$\theta^{\text{Rach approach}}_{\text{Convective tip}}$	Error
0.00	1.000000	1.000000	0.000000
0.10	0.9244397050496332	0.924439719876500	1.48×10^{-8}
0.20	0.8592298683746248	0.859229856797000	1.15×10^{-8}
0.30	0.8017755568158551	0.801775545683500	1.11×10^{-8}
0.40	0.7501074942614540	0.750107487643230	6.61×10^{-9}
0.50	0.7026671620195272	0.702667157809430	4.21×10^{-9}
0.60	0.6581697277354990	0.658169734578900	6.84×10^{-9}
0.70	0.6155134680018295	0.615513476590870	8.58×10^{-9}
0.80	0.5737184198747134	0.573718423657900	3.78×10^{-9}
0.90	0.5318844255441258	0.531884439876589	1.43×10^{-8}
1.00	0.4891629397952363	0.489162946560900	6.76×10^{-9}

and 4 depict the numerical values of dimensionless temperature $\theta(\eta)$ for an insulated-tip and convective-tip boundary conditions, respectively when: $n = 1, m = 3, \varphi_{GO} = \varphi_{MoS_2} = 2\%, Nc = 1, Nr = 1, \theta_a = 0.2, m_2 = 1$ and $Bi = 1$. These tables also demonstrate the higher efficiency of DRA method when compared to the numerical RKFT45 used as a guide. The error is introduced as follows:

$$Error = |\theta^{DRA} - \theta^{RKFT45}|$$

5. Concluding remarks

In this research work we have studied the influence of thermal radiative and free convective flowing of hybrid nanofluid over a moving porous longitudinal fin by considering two types of boundary conditions: insulated tip and convective tip. This investigation treated the nonlinear governing equation numerically and analytically via RKFT45 and Duan–Rach Approach respectively for different values of physical quantities of interest like a radiative parameter, ambient temperature, Peclet number, wet porous parameter, Biot number, and power index parameter. It is found that the dimensionless temperature $\theta(\eta)$ decreases with the augment of radiative parameter *Nr*, wet porous number m_2 and convective parameter *Nc* in the cases of insulated and convective tips; however, the temperature $\theta(\eta)$ increases with the rise in the magnitude of ambient temperature θ_a, Peclet number *Pe* and power index *n*. It is also found that the thermal profile $\theta(\eta)$ presents a decrease for all considered shape factors in the cases of insulated and convective tips boundary conditions. Otherwise, results obtained reveal that the temperature decreases as the Biot number *Bi* increases.

From the comparison, the gained results with DRA method agree very well with those available in literature in which is shown the dependence of dimensionless temperature $\theta(\eta)$ with the Peclet number, *Pe*. It is also established that the heat transmission rate $-\theta'(0)$ appears as a decreasing function of *Pe* for a given value of a wet porous number m_2. This decline is sharpest in the case of convective-tip boundary condition when compared to that stated in the case of insulated-tip bounder constraints.

Disclosure statement

No potential conflict of interest was reported by the author(s).

ORCID

Mohamed R. Eid http://orcid.org/0000-0003-2479-9809

References

[1] Taylor R, Coulombe S, Otanicar T, et al. Small particles, big impacts: a review of the diverse applications of nanofluids. J Appl Phys. 2013;113(1):1.
[2] Buongiorno J. Convective transport in nanofluids. J Heat Transfer. 2006;128(3):240–250.
[3] Minkowycz W, Sparrow EM, Abraham JP. Nanoparticle heat transfer and fluid flow. Milton Park: CRC Press, Taylor & Francis; 2013.
[4] Das SK, Choi SU, Yu W, et al. Nanofluids: science and technology. Hoboken, NJ: Wiley; 2007.
[5] Kakaç S, Pramuanjaroenkij A. Review of convective heat transfer enhancement with nanofluids. Int J Heat Mass Transf. 2009;52(13–14):3187–3196.
[6] Alizadeh M, Dehghan A. Conjugate natural convection of nanofluids in an enclosure with a volumetric heat source. Arab J Sci Eng. 2014;39(2):1195–1207.
[7] Kuznetsov A, Nield D. Natural convective boundary-layer flow of a nanofluid past a vertical plate. Int J Therm Sci. 2010;49(2):243–247.
[8] Mintsa HA, Roy G, Nguyen CT, et al. New temperature dependent thermal conductivity data for water-based nanofluids. Int J Therm Sci. 2009;48(2):363–371.
[9] Madhesh D, Kalaiselvam S. Experimental study on the heat transfer and flow properties of Ag–ethylene glycol nanofluid as a coolant. Heat Mass Transf. 2014;50(11):1597–1607.
[10] Shi L, Hu Y, He Y. Magneto-responsive thermal switch for remote-controlled locomotion and heat transfer based on magnetic nanofluid. Nano Energy. 2020;71:104582.
[11] Katam M, Ganganapalli S, Kata S, et al. Coupled effect of multi-slips and activation energy in a micropolar nanoliquid on a convectively heated elongated surface. Heat Transf Asian-Res. 2021;50(6):6237–6258.
[12] Satya Narayana PV, Tarakaramu N, Harish Babu D. Influence of chemical reaction on MHD couple stress nanoliquid flow over a bidirectional stretched sheet. Int J Ambient Energy. 2021. DOI:10.1080/01430750.2021.1923569
[13] Satya Narayana PV, Tarakaramu N, Sarojamma G, et al. Numerical simulation of nonlinear thermal radiation on the 3D flow of a couple Casson nanofluid due to a stretching sheet. J Therm Sci Eng Appl. 2021;13(2):021028.
[14] Abd Elazem NY, Elgazery NS. Unsteady radiative nanofluid flow near a vertical heated wavy surface with temperature-dependent viscosity. Chin J Phys. 2021;74:38–52.
[15] Hussain F, Hussain A, Nadeem A. Unsteady shear thining behavior of nanofluid flow over exponential stretching/shrinking cylinder. J Mol Liq. 2022;345:117894.
[16] Kumaraswamy Naidu K, Harish Babu D, Harinath Reddy S, et al. Radiation and partial slip effects on magnetohydrodynamic Jeffrey nanofluid containing gyrotactic microorganisms over a stretching surface. J Therm Sci Eng Appl. 2021;13(3):031011.
[17] Sarkar J, Ghosh P, Adil A. A review on hybrid nanofluids: recent research, development and applications. Renew Sustain Energy Rev. 2015;43:164–177.
[18] Jana S, Salehi-Khojin A, Zhong W-H. Enhancement of fluid thermal conductivity by the addition of single and hybrid nano-additives. Thermochim Acta. 2007;462(1–2):45–55.
[19] Ghadikolaei S, Yassari M, Sadeghi H, et al. Investigation on thermophysical properties of TiO_2–Cu/H_2O hybrid nanofluid transport dependent on shape factor in MHD stagnation point flow. Powder Technol. 2017;322:428–438.
[20] Iqbal Z, Maraj E, Azhar E, et al. A novel development of hybrid (MoS_2-SiO_2/H_2O) nanofluidic curvilinear transport and consequences for effectiveness of shape factors. J Taiwan Inst Chem Eng. 2017;81:150–158.

[21] Nawaz M, Nazir U. An enhancement in thermal performance of partially ionized fluid due to hybrid nano-structures exposed to magnetic field. AIP Adv. 2019;9(8):085024.
[22] Chu Y-M, Nisar KS, Khan U, et al. Mixed convection in MHD water-based molybdenum disulfide-graphene oxide hybrid nanofluid through an upright cylinder with shape factor. Water (Basel). 2020;12(6):1723.
[23] Venkateswarlu B, Satya Narayana PV. Cu-Al_2O_3 hybrid nanofluid flow past a porous stretching sheet due to temperatura-dependent viscosity and viscous dissipation. Heat Transf Asian-Res. 2020;50(1):432–449.
[24] Wakif A, Animasaun IL, Satya Narayana PV, et al. Meta-analysis on thermo-migration of tiny/nano-sized particles in the motion of various fluids. Chin J Phys. 2020;68:293–307.
[25] Basir MFM, Mabood F, Satya Narayana PV, et al. Significance of viscous dissipation on the dynamics of ethylene glycol conveying diamond and silica nanoparticles through a diverging and converging channel. J Therm Anal Calorim. 2020. DOI:10.1007/s10973-020-10335-4
[26] Ramzan M, Mehmood T, Alotaibi H, et al. Comparative study of hybrid and nanofluid flows amidst two rotating disks with thermal stratification: statistical and numerical approach. Case Stud Therm Eng. 2021;28:101596.
[27] Rajesh V, Sheremet MA, Oztop HF. Impact of hybrid nanofluids on MHD flow and heat transfer near a vertical plate with ramped wall temperature. Case Stud Therm Eng. 2021;28:101557.
[28] Eid MR, Al-Hossainy AF. Combined experimental thin film, DFT-TDDFT computational study, flow and heat transfer in [PG-MoS_2/ZrO_2]^C hybrid nanofluid. Waves Random Complex Media. 2021:1–26. DOI:10.1080/17455030.2021.1873455
[29] Al-Hossainy AF, Eid MR. Combined experimental thin films, TDDFT-DFT theoretical method, and spin effect on [PEG-H_2O/ZrO_2+MgO] h hybrid nanofluid flow with higher chemical rate. Surf Interfaces. 2021;23:100971.
[30] Eid MR, Al-Hossainy AF. High-performance nanofluid synthesis and DFT-TDDFT study of graphene nanosheets along bent surface for enhanced oil-recovery implementations. Case Stud Therm Eng. 2021;25:100983.
[31] Duan J-S, Rach R. A new modification of the Adomian decomposition method for solving boundary value problems for higher order nonlinear differential equations. Appl Math Comput. 2011;218(8):4090–4118.
[32] Kezzar M, Boumaiza N, Tabet I, et al. Combined effects of ferromagnetic particles and magnetic field on mixed convection in the Falkner-Skan system using DRA. Int J Numer Methods Heat Fluid Flow. 2019;29(2):814–832.
[33] Gahgah M, Sari MR, Kezzar M, et al. Duan–Rach modified Adomian decomposition method (DRMA) for viscoelastic fluid flow between nonparallel plane walls. Eur Phys J Plus. 2020;135(2):1–17.
[34] Kezzar M, Tabet I, Eid MR. A new analytical solution of longitudinal fin with variable heat generation and thermal conductivity using DRA. Eur Phys J Plus. 2020;135(1):1–15.
[35] Fenizri W, Kezzar M, Sari MR, et al. New modified decomposition method (DRMA) for solving MHD viscoelastic fluid flow: comparative study. Int J Ambient Energy. 2020:1–9. DOI:10.1080/01430750.2020.1852114
[36] Gireesha B, Sowmya G, Khan MI, et al. Flow of hybrid nanofluid across a permeable longitudinal moving fin along with thermal radiation and natural convection. Comput Methods Programs Biomed. 2020;185:105166.